



HAL
open science

4D Thermomechanical metamaterials for soft microrobotics

Qingxiang Ji, Johnny Moughames, Xueyan Chen, Guodong Fang, Juan Huaroto, Vincent Laude, Julio Andrés Iglesias Martínez, Gwenn Ulliac, Cédric Clévy, Philippe Lutz, et al.

► **To cite this version:**

Qingxiang Ji, Johnny Moughames, Xueyan Chen, Guodong Fang, Juan Huaroto, et al.. 4D Thermomechanical metamaterials for soft microrobotics. *Communications Materials*, 2021, 2 (1), pp.93. 10.1038/s43246-021-00189-0 . hal-04274268

HAL Id: hal-04274268

<https://cnrs.hal.science/hal-04274268>

Submitted on 7 Nov 2023

HAL is a multi-disciplinary open access archive for the deposit and dissemination of scientific research documents, whether they are published or not. The documents may come from teaching and research institutions in France or abroad, or from public or private research centers.

L'archive ouverte pluridisciplinaire **HAL**, est destinée au dépôt et à la diffusion de documents scientifiques de niveau recherche, publiés ou non, émanant des établissements d'enseignement et de recherche français ou étrangers, des laboratoires publics ou privés.

4D Thermomechanical metamaterials for soft microrobotics

Qingxiang Ji ^{1,2}, Johnny Moughames², Xueyan Chen^{1,2}, Guodong Fang¹, Juan J. Huaroto², Vincent Laude ², Julio Andrés Iglesias Martínez², Gwenn Ulliac², Cédric Clévy ², Philippe Lutz², Kanty Rabenorosoa², Valerian Guelpa², Arnaud Spangenberg^{3,4}, Jun Liang ⁵✉, Alexis Mosset ² & Muamer Kadic²✉

Metamaterials have attracted wide scientific interest to break fundamental bounds on materials properties. Recently, the field has been extending to coupled physical phenomena where one physics acts as the driving force for another. Stimuli-responsive or 4D metamaterials have been demonstrated for thermo-elasticity, magneto-optics or piezo-electricity. Herein, a soft, ultra-compact and accurate microrobot is described which can achieve controlled motion under thermal stimuli. The system consists of an organized assembly of two functional structures: a rotational and a translational element. Both elements are designed basing upon the principle of the thermoelastic bilayer plate that bends as temperature changes. Samples are fabricated using gray-tone lithography from a single polymer but with two different laser writing powers, making each part different in its thermal and mechanical behaviors. Excellent motion-controllable, reversible and stable features in a dry environment are verified by simulations and experiments, revealing broad application prospects for the designed soft micro actuators.

¹National Key Laboratory of Science and Technology on Advanced Composites in Special Environments, Harbin Institute of Technology, Harbin, China.

²Institute FEMTO-ST, CNRS, University Bourgogne Franche-Comté, Besançon, France. ³Université de Haute-Alsace, CNRS, IS2M UMR 7361, Mulhouse, France. ⁴Université de Strasbourg, Strasbourg, France. ⁵Institute of Advanced Structure Technology, Beijing Institute of Technology, Beijing, China.

✉email: liangjun@bit.edu.cn; muamer.kadic@univ-fcomte.fr

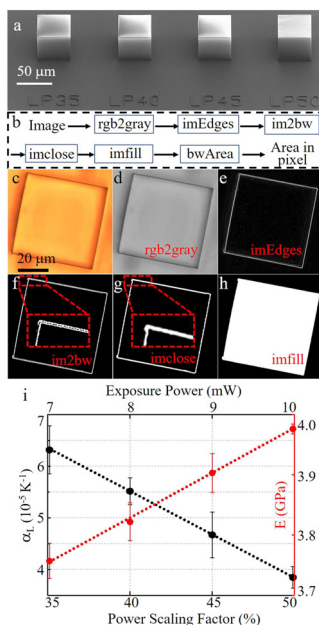


Fig. 2 CTE and Young's modulus measurement. **a** Bulk polymer cubes written by different laser power scaling factors. **b** Outline of the general process in ImageJ to obtain areas measured in pixels: the optical image of a polymer cube in panel **(c)** is first converted into 8-bit format in panel **(d)**. Then an edge detection algorithm is applied and the image is converted into a binary image in panel **(e)**. After applying closing algorithms in panel **(f)** and filling algorithms in panel **(g)**, we finally obtain the internal area defined by these edges in panel **(h)**. **i** The CTE versus laser exposure power is obtained by measuring areas before and after heating. The Young's modulus depicted in red is measured by Brillouin light scattering metrology. The bottom horizontal axis gives the power scaling factor whereas the top horizontal axis gives the actual power. We add black (red) error bars to indicate standard deviations of the calculated CTE (Young's modulus). The CTE decreases (Young's modulus increases) with the laser exposure power. Both variations are approximately linear.

the edges (see Fig. 2f, g). Finally, based on the obtained areas measured in pixels, we estimate the CTE following

$$\alpha_L = \frac{A_f - A_b}{2A_b \Delta T} \quad (1)$$

where A_b and A_f are the areas obtained from images captured before and after heating, respectively. The correlation between the CTE and the laser exposure power is established in Fig. 2i. We observe that the CTE decreases approximately linearly with the laser exposure power.

The mechanical properties (here Young's modulus E) for different laser powers are also obtained by measuring the aforementioned bulk polymer cuboid samples. We use Brillouin light scattering to measure the longitudinal elastic modulus from which we obtain Young's modulus (see Supplementary Fig. 2 and Supplementary Mechanical Properties Measurement). We observe quasi-linear dependence of Young's modulus on the laser exposure power, as increasing laser power results in enhanced photopolymerization and therefore increased stiffness^{35,36}. It is noted that only the ratio E_1/E_2 actually enters into the effective deformation of bimaterial beams⁸.

As a proof of demonstration, we fabricate bilayer beams with two components defined by two different power scaling factors and beams with a single component for comparison (see Supplementary Fig. 3 and Supplementary Fabrication Technique). Observations show that the two-component beams deform and bend as the surrounding temperature changes, but also that

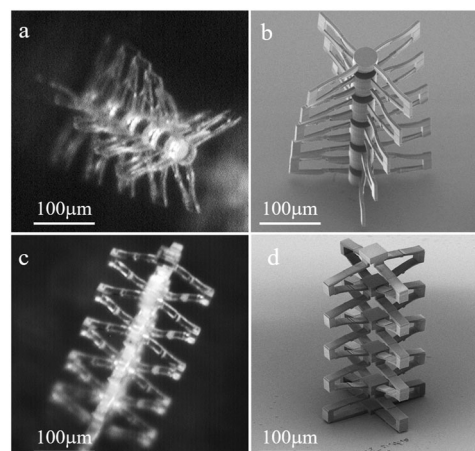


Fig. 3 Functional stacks fabricated by gray-tone lithography. **a, c** Optical micrographs and **b, d** SEM images. Each stack is composed of five elements. The samples are composed of two constituent components fabricated with a single photoresist but two different laser exposure powers. Differential shrinkage during development leads to pre-bending of the bilayer beams, further leading to rotation (translation) of the stack shown in the panels.

they shrink during development, whereas the single-component beams are almost not influenced by temperature variations, demonstrating that the two components indeed have different properties. We thereby safely validate the fabrication strategy and demonstrate the possibility of printing a microrobot in only one step using a single photoresist and gray-tone lithography.

Based on the above laser writing strategy, we fabricate the metamaterials depicted in Fig. 1 using a single photoresist but two laser writing powers. We construct the less active component with a laser power 10 mW and the more active component with a laser power 9 mW. Clearly, a larger difference in selected power scaling factors would bring in larger motional amplitudes; however, it would also add more difficulties during fabrication and would specially lead to less repeatable motions for poorly exposed polymers. Here, we aim at designing a repeatable response and thus we must use the less damageable material. Poorly exposed polymer structures are indeed porous, they shrink a lot and they are thus not resistant to ambient conditions. With the chosen power scaling factors the fabricated samples show better mechanical stability and fewer imperfections. Optical and scanning electron microscopy (SEM) micrographs of selected fabricated stacks are shown in Fig. 3. We stress that the built components look alike in optical and electronic images, but that they are actually different in their thermal and mechanical properties. We notice the pre-bending of bimaterial beams, which originates from different volume shrinkage during the development process. Within the linear regime, this pre-bending does not change the thermal operation. Instead, it directly evidences that the two components with different exposure powers are different in their thermal and mechanical properties. We can also notice the rotation (or translation) that results from pre-bending, in agreement with the designed operation principle.

Characterization of the thermally responsive behavior. To test the concept, we discuss the actuating performance of the functional stacks (see Supplementary Fig. 4 and Supplementary Conceptual Testing). Upon electron beam heating (for about 10 s), the structures exhibit a thermal-mechanical response with corresponding motion. We wait for a given time (here 60 min) for the environment and the samples to naturally cool back to the initial temperature. Note that such long cooling times are needed due to

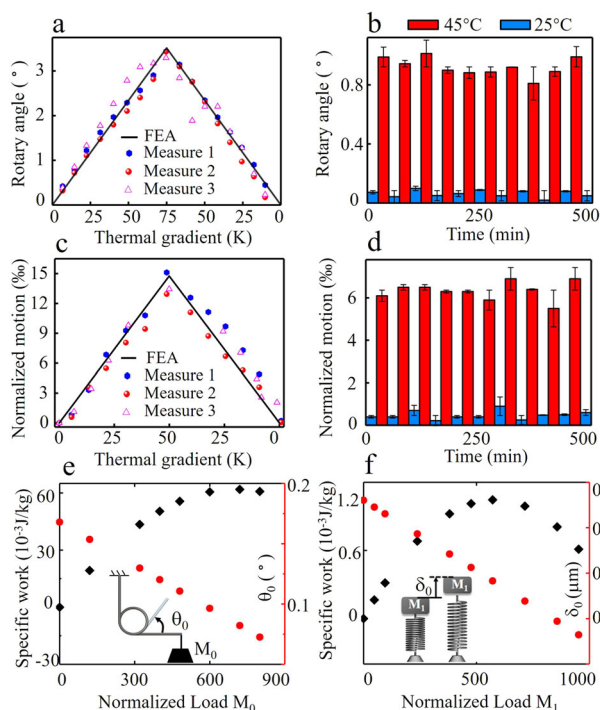


Fig. 4 Temperature-dependent measurement of the fabricated stacks. **a, c** Dependence of motional amplitudes of the stacks with the thermal gradient for rotation and translation, respectively. The plots show a symmetric, linear, and reversible amplitude response. **b, d** Cyclic stability of the structures for rotation and translation, respectively, where temperatures are switched between 25 °C (marked in blue) and 45 °C (marked in red). The error bars (marked in black) indicate the difference between experimental and numerical results. Note that the translational displacements in panels (**c–d**) are normalized to the initial non-heated stack length in the z-direction. **e, f** The specific work (i.e., the work normalized to the mass of the structure) and the actuation motion of the elements under thermal stimuli are plotted versus the normalized load and represented in analogy with Hooke's springs shown in the insets. Loads M_0 and M_1 have been normalized by the mass of the rotational element (2.5×10^{-10} kg) and translational element (2.1×10^{-10} kg), respectively. A linear relationship between displacements and external loads is observed in both cases, suggesting that the elastic limit is not reached.

the absence of active cooling. When external heating is released, motion gradually decreases until the initial rest point is retrieved. Such an observation suggests that the thermal-driven behavior is sensitive and reversible.

In order to evaluate quantitatively the thermally induced actuation mechanism, we conduct finite element analysis (FEA) and temperature-dependent measurements to check whether the structures behave exactly as designed. For FEA, we use the commercial software COMSOL Multiphysics. In the experiments, the structures are heated in an enclosed chamber with well-controlled temperatures. We apply image cross-correlation analysis to obtain the temperature-induced displacement field and hence reveal the motion mechanism. Figure 4a, c summarizes the temperature-dependent measurement results, where temperatures are elevated gradually from 21.8 to 96.4 °C (with temperature difference around 75 K) for the thermally induced rotation behavior and temperatures are elevated gradually from 21.8 to 71.7 °C (with temperature difference around 50 K) for the thermally induced translation behavior, respectively. It is observed that the rotational and translational amplitudes increase linearly with the thermal gradient, in good agreement with FEA. Desired motional amplitudes can hence be accurately achieved by

applying predefined temperature variations. Besides, motional amplitudes decrease to zero as the temperature returns to its initial value, revealing a well reversible performance. These results quantitatively demonstrate that the designed structures feature an accurate and reversible behavior under thermal stimuli. Movies of rotation (Supplementary Movie 2) and translation (Supplementary Movie 3) under thermal stimuli are available in the Supplementary Information. We can observe minor differences between the measured results and the FEA results. The uncertainty mainly originates from the inaccuracy of the measured CTE and Young's moduli. Imperfections of the fabricated samples also add to these differences. For example, due to a drift during writing, the two layers in some of the bimaterial beams may not be well connected, even to the extent of detaching.

To check the robustness of the thermally driven operation, we test the functional stack under several heating-and-cooling cycles. Both the heating process and the cooling process last for 25 min during each cycle, ensuring that the system can reach its steady state. Hence, the full cycle time of a reversible switch is 50 min for the thermal cycling conditions used. As shown in Fig. 4b, the rotation angle changes from around 0.08° to 0.92° as temperatures are switched from 25 to 45 °C. This actuation is reversible and repeatable upon several heating-and-cooling cycles, and the thermally induced motional amplitudes are stable with small deterioration, which demonstrates a predictable long and stable working life. Similar relations of translational stacks are also observed in Fig. 4d. One may raise concerns regarding the small motion produced by the samples. In this work, the samples are fabricated to demonstrate extremely accurate and reversible operation, at the sacrifice of motional amplitudes. However, the observed motion is still comparable to what has been reported in the literatures for micro-structured thermally responsive metamaterials in a dry environment⁸ and it has to be emphasized that actuation is remotely controlled and does not rely on an external mechanical actuation as is often the case. We investigated by numerical simulation the relationship between motional amplitudes and constructed parameters (see Supplementary Fig. 5 and Supplementary Parameter Analysis). It is found that the amplitudes can be effectively adjusted by tuning structural and material parameters, or imposing larger temperature variations.

We finally estimate the potential torque (or force) that the designed structures can produce to move an object. The analysis of mechanical responses requires the correlation of the motional amplitude to an external load. Thereby, we use numerical calculations with the commercial software COMSOL Multiphysics. In our simulations, we consider a rotational (or translational) element with a torque (or force) applied to the sideways surface (or to the top end) in the opposite direction to the thermally induced displacement. A temperature elevation of 20 K is then imposed. Motional amplitudes are obtained versus increasing weight loading. The load-carrying capability is characterized by the applied load and by the specific work that the elements produce under the temperature elevation. The rotational (translational) elements work like Hooke's torsion (linear) springs by twisting (pushing) the end along its axis. Specifically, when a rotational (translational) element undergoes a temperature elevation, it exerts a torque (force) on external objects that is proportional to the angle (displacement), in analogy with a spring in a twisted (compressed) state (see the insets in Fig. 4e, f). Note that the torsion (linear) spring strictly obeys Hooke's law, as the elastic limit is not reached in this work (see Supplementary Figs. 6 and 7 and Supplementary Actuation Performance).

With increasing weight loading, the actuation angle (displacement) decreases linearly while the specific work first increases to the maximum value of $59 \times 10^{-3} \text{ J kg}^{-1}$ ($1.1 \times 10^{-3} \text{ J kg}^{-1}$) and then decreases gradually. Importantly, elements with a

temperature elevation $\Delta T = 20$ K can offer a considerable actuation torque (or force) that is able to move roughly 1000 times their own weight (see Fig. 4e, f). The results are comparable with the characterization results in literature³² in which, however, only contraction at the millimeter scale are demonstrated. Note that one can obtain larger actuation torque (or force) by simply imposing larger temperature variations or by adjusting construction parameters.

Conclusion. In summary, we have developed thermomechanical metamaterials that achieve elementary motions (rotation and translation) under thermal stimuli and can further assemble into a three-axis microrobot. The thermally driven behavior is obtained in a controlled manner and in a dry environment. The proposed metamaterials are fabricated using a single polymer but two different laser writing powers, thus making each part different in its thermal and mechanical properties. We verified that the designed compact metamaterials show accurate, stable, and reversible response through numerical simulations and experiments. Their operation can be easily and accurately controlled by external thermal sources, with great potential in microrobotics and other related domains.

Methods

Samples design. The thermally actuated structures are based on bilayer beams, utilizing the different thermal and mechanical properties of two different layers. To obtain the maximum thermally induced motion and hence the best actuation performance, optimization was conducted on the bilayer beams. Instead of a simple single bimaterial beam, a S-shaped pattern was chosen. For a single bilayer beam under a thermal stimulus, both axial and tangential movements are induced. The end of a bilayer beam will be tilted (see Supplementary Fig. 8a). Such a tilt angle at the end of the bilayer beams significantly reduces the effective motional amplitude of the whole structure. If two bilayer beams with inverted layer compositions are connected to form a S-shaped beam, the tilt angle at the end of the second beam is compensated for (see Supplementary Fig. 8b and Supplementary Sample Design)³⁷. An overlap part was added to connect the two inverted bilayer beams, making the structures mechanically more robust. Besides, the overlap part largely facilitates the fabrication process.

Samples fabrication. The rotational and translational stacks were both assembled in the z -direction by 5 elements. Samples were fabricated using a negative tone photoresist (IP-Dip, Nanoscribe GmbH) and a commercial 3D gray-tone two-photon lithography system (Photonics Professional, Nanoscribe GmbH). A drop of resin was deposited on a fused silica substrate with dimensions $25 \times 25 \times 0.7$ mm³ and photopolymerized with a femtosecond laser operating at $\lambda = 780$ nm. After printing, the sample was developed for 20 min in Propylene glycol methyl ether acetate (PGMEA) solution to remove the unexposed photoresist and rinsed for 3 min in Isopropyl alcohol (IPA) to clear the developer. In the fabrication process, the more active component was first fabricated with a laser power 9 mW. Then the laser was drifted and another component was fabricated with a laser power 10 mW. A Galvanometric scan speed of 10 mm s⁻¹ was used for the whole fabrication process. Key material properties and geometry sizes of the samples are listed in Fig. 1.

Temperature-dependent characterization. During the measurements, the samples were placed on a flat heater within an encapsulated chamber. In this manner, the samples, as well as the air within the chamber, were heated by the heater. After a certain time (here we chose 25 min), we assumed that the system reached its steady state and that the sample temperature was uniform and stable which was actually equal to the surrounding air temperature. The heating processes were controlled by a commercial Linkam system, ranging from 25 to 100 °C. For accuracy, we placed a calibrated thermo-sensor at the sample location and recorded live temperatures during each heating process. The chamber had a glass window on the top end, allowing for optical access and imaging by an optical microscope. Images were acquired using a single microscope lens (Achromplan 20 \times with a numerical aperture NA = 0.4) via a charge-coupled-device (CCD) camera. The samples were moved with respect to the microscope by manually moving the entire chamber using a translation stage. For each sample, we observed them for at least three times.

Data availability

The data that support the findings of this study are available from the corresponding authors on reasonable request.

Received: 6 April 2021; Accepted: 7 July 2021;

Published online: 09 September 2021

References

1. Florijn, B., Coulais, C. & van Hecke, M. Programmable mechanical metamaterials. *Phys. Rev. Lett.* **113**, 175503 (2014).
2. Christensen, J., Kadic, M., Kraft, O. & Wegener, M. Vibrant times for mechanical metamaterials. *MRS Commun.* **5**, 453–462 (2015).
3. Kadic, M., Milton, G. W., van Hecke, M. & Wegener, M. 3D metamaterials. *Nat. Rev. Phys.* **1**, 198–210 (2019).
4. Zangeneh-Nejad, F., Sounas, D. L., Alù, A. & Fleury, R. Analogue computing with metamaterials. *Nat. Rev. Mater.* **6**, 1–19 (2020).
5. Fleury, R., Sounas, D. L., Sieck, C. F., Haberman, M. R. & Alù, A. Sound isolation and giant linear nonreciprocity in a compact acoustic circulator. *Science* **343**, 516–519 (2014).
6. Kadic, M., Schittny, R., Bückmann, T., Kern, C. & Wegener, M. Hall-effect sign inversion in a realizable 3D metamaterial. *Phys. Rev. X* **5**, 021030 (2015).
7. Koschny, T., Soukoulis, C. M. & Wegener, M. Metamaterials in microwaves, optics, mechanics, thermodynamics, and transport. *J. Opt.* **19**, 084005 (2017).
8. Qu, J., Kadic, M., Naber, A. & Wegener, M. Micro-structured two-component 3D metamaterials with negative thermal-expansion coefficient from positive constituents. *Sci. Rep.* **7**, 40643 (2017).
9. Spiegel, C. A. et al. 4D printing at the microscale. *Adv. Funct. Mater.* **30**, 1907615 (2019).
10. Hippler, M. et al. Controlling the shape of 3D microstructures by temperature and light. *Nat. Commun.* **10**, 1–8 (2019).
11. Hippler, M. et al. 3D scaffolds to study basic cell biology. *Adv. Mater.* **31**, 1808110 (2019).
12. Gernhardt, M. et al. Tailoring the mechanical properties of 3D microstructures using visible light post-manufacturing. *Adv. Mater.* **31**, 1901269 (2019).
13. Coulais, C., Sounas, D. & Alù, A. Static non-reciprocity in mechanical metamaterials. *Nature* **542**, 461–464 (2017).
14. Brandenbourger, M., Locsin, X., Lerner, E. & Coulais, C. Non-reciprocal robotic metamaterials. *Nat. Commun.* **10**, 1–8 (2019).
15. Rafsanjani, A., Bertoldi, K. & Studart, A. R. Programming soft robots with flexible mechanical metamaterials. Preprint at <https://arxiv.org/abs/1906.00306> (2019).
16. Mirzaali, M., Janbaz, S., Strano, M., Vergani, L. & Zadpoor, A. A. Shape-matching soft mechanical metamaterials. *Sci. Rep.* **8**, 1–7 (2018).
17. Hippler, M. et al. Mechanical stimulation of single cells by reversible host-guest interactions in 3D microscavolds. *Sci. Adv.* **6**, eabc2648 (2020).
18. Acome, E. et al. Hydraulically amplified self-healing electrostatic actuators with muscle-like performance. *Science* **359**, 61–65 (2018).
19. Amjadi, M. & Sitti, M. Self-sensing paper actuators based on graphite-carbon nanotube hybrid films. *Adva. Sci.* **5**, 1800239 (2018).
20. Liu, Z. et al. Hierarchically buckled sheath-core fibers for superelastic electronics, sensors, and muscles. *Science* **349**, 400–404 (2015).
21. Shi, Q. et al. A remote controllable fiber-type near-infrared light-responsive actuator. *Chem. Commun.* **53**, 11118–11121 (2017).
22. Han, D.-D. et al. Light-mediated manufacture and manipulation of actuators. *Adv. Mater.* **28**, 8328–8343 (2016).
23. Haines, C. S. et al. Artificial muscles from fishing line and sewing thread. *Science* **343**, 868–872 (2014).
24. Chin, S. M. et al. Covalent-supramolecular hybrid polymers as muscle-inspired anisotropic actuators. *Nat. Commun.* **9**, 1–11 (2018).
25. Han, D.-D. et al. Moisture-responsive graphene paper prepared by self-controlled photoreduction. *Adv. Mater.* **27**, 332–338 (2015).
26. Castaldo, R. et al. Humidity-driven mechanical and electrical response of graphene/cloisite hybrid films. *Adv. Funct. Mater.* **29**, 1807744 (2019).
27. Lee, S.-W., Prosser, J. H., Purohit, P. K. & Lee, D. Bioinspired hygromorphic actuator exhibiting controlled locomotion. *ACS Macro Lett.* **2**, 960–965 (2013).
28. Tottori, S. et al. Magnetic helical micromachines: fabrication, controlled swimming, and cargo transport. *Adv. Mater.* **24**, 811–816 (2012).
29. Li, K. et al. Tunable magnetic response in 2d materials via reversible intercalation of paramagnetic ions. *Adv. Electron. Mater.* **5**, 1900040 (2019).
30. Magdanz, V., Sanchez, S. & Schmidt, O. G. Development of a sperm-flagella driven micro-bio-robot. *Adv. Mater.* **25**, 6581–6588 (2013).
31. Wang, J. & Gao, W. Nano/microscale motors: biomedical opportunities and challenges. *ACS Nano* **6**, 5745–5751 (2012).
32. Kotikian, A., Truby, R. L., Boley, J. W., White, T. J. & Lewis, J. A. 3d printing of liquid crystal elastomeric actuators with spatially programed nematic order. *Adv. Mater.* **30**, 1706164 (2018).
33. Huang, T.-Y. et al. Four-dimensional micro-building blocks. *Sci. Adv.* **6**, eaav8219 (2020).

34. Jiang, W. et al. Photoresponsive soft-robotic platform: biomimetic fabrication and remote actuation. *Adv. Funct. Mater.* **24**, 7598–7604 (2014).
35. Rys, J., Steenhusen, S., Schumacher, C., Cronauer, C. & Daraio, C. Locally addressable material properties in 3D micro-architectures. *Extreme Mech. Lett.* **28**, 31–36 (2019).
36. Lemma, E. D. et al. Mechanical properties tunability of three-dimensional polymeric structures in two-photon lithography. *IEEE Trans. Nanotechnol.* **16**, 23–31 (2016).
37. Jia, K., Pal, S. & Xie, H. An electrothermal tip-tilt-piston micromirror based on folded dual S-shaped bimorphs. *J. Microelectromech. Syst.* **18**, 1004–1015 (2009).

Acknowledgements

This work was supported by the EIPHI Graduate School [grant number ANR-17-EURE-0002], the French Investissements d’Avenir program, project ISITEBFC [grant number ANR-15-IDEX-03], and the National Natural Science Foundation of China [grant numbers 11732002 and 11672089]. This work was supported by the french RENATECH network and its FEMTO-ST technological facility.

Author contributions

Q.J. and M.K. conceived the idea. Q.J., X.C., and J.A.I. performed numerical simulations. J.M. and G.U. fabricated the samples and obtained optical and SEM images. Q.J., J.A.I., J.J.H., and A.M. designed and implemented the experiments. Q.J., G.F., J.J.H., V.L., V.G., A.S., A.M., and M.K. analyzed the data and discussed the results. Q.J., G.F., V.L., C.C., P.L., K.R., A.S., J.L., and M.K. prepared the manuscript. M.K. and J.L. supervised the overall project. All the authors contributed to the discussion and to finalizing the manuscript.

Competing interests

The authors declare no competing interests.

Additional information

Supplementary information The online version contains supplementary material available at <https://doi.org/10.1038/s43246-021-00189-0>.

Correspondence and requests for materials should be addressed to J.L. or M.K.

Peer review information *Communications Materials* thanks Teunis van Manen and the other, anonymous, reviewer(s) for their contribution to the peer review of this work. Primary Handling Editors: Aldo Isidori.

Reprints and permission information is available at <http://www.nature.com/reprints>

Publisher’s note Springer Nature remains neutral with regard to jurisdictional claims in published maps and institutional affiliations.



Open Access This article is licensed under a Creative Commons Attribution 4.0 International License, which permits use, sharing, adaptation, distribution and reproduction in any medium or format, as long as you give appropriate credit to the original author(s) and the source, provide a link to the Creative Commons license, and indicate if changes were made. The images or other third party material in this article are included in the article’s Creative Commons license, unless indicated otherwise in a credit line to the material. If material is not included in the article’s Creative Commons license and your intended use is not permitted by statutory regulation or exceeds the permitted use, you will need to obtain permission directly from the copyright holder. To view a copy of this license, visit <http://creativecommons.org/licenses/by/4.0/>.

© The Author(s) 2021